Ground-layer adaptive-optics system modelling for the Chinese
Large Optical/Infrared Telescope

Peng Jia,[1,2]★ Alastair Basden[2]★ and James Osborn[2]

[1]*College of Physics and Optoelectronics, Taiyuan University of Technology, Taiyuan, 030024, China*
[2]*Department of Physics, Durham University, South Road, Durham DH1 3LE, UK*

ABSTRACT

The Chinese *Large Optical/Infrared Telescope* is currently undergoing design studies. A ground-layer adaptive-optics system (GLAO) has been proposed, with a 14 -arcmin field of view (FOV) and moderate adaptive-optics correction using a deformable secondary mirror, several laser guide stars (LGS) and wavefront sensors. Due to its large FOV and relatively complex structure, some important problems should be analysed to aid budget considerations for the whole telescope. In this paper, we propose a FOV-related evaluation factor to describe the GLAO performance and use an end-to-end Monte Carlo simulation to test its performance under different configurations. To accelerate the parameter space exploration speed, we split the parameter space of the GLAO system and apply a bottom-up search procedure for parameter selection. We also propose a simplified turbulence geometric model to evaluate the GLAO performance with different turbulence-profile-related parameters. With the above methods, we analyse the required number of deformable mirror (DM) actuators, the number, position and magnitude of LGS and explore the DM tilt-conjugation problem for this GLAO system.

Key words: instrumentation: adaptive optics – methods: numerical – telescopes.

1 INTRODUCTION

A 12-m telescope called the Chinese *Large Optical/Infrared Telescope* (*LOT*) has been proposed by a collaboration based in China, for optical and infra-red astronomical observations (Cui & Zhu 2016; Su et al. 2016). It is a large-aperture general-purpose telescope with a segmented primary mirror with a diameter of 12 m and an f-ratio of 1.6. To feed different pieces of back-end equipment, this telescope has a prime focus, Cassegrain, Nasmyth and coudé systems. In previous studies, the optical design and some of the preliminary considerations of adaptive optics (AO) for *LOT* were discussed, and the final suggestion for its optical system was given. The chosen design has four mirrors with an SYZ relay system (Su, Yu & Zhou 1990), and the secondary mirror will be used as a deformable mirror (DM) by the AO systems (Su et al. 2017).

One of the major tasks for the secondary deformable mirror is to provide moderate and uniform AO correction for the Nasmyth instruments in a 14-arcmin field of view (FOV). In that system, many wide-field observations will be carried out, including velocity field surveys at galactic scales, high-accuracy astrometry and photometry of stars, direct imaging of gravitational arcs, galaxies, fast-moving objects and the discovery of faint transit objects. These observations require uniform and improved image quality in a relatively large

FOV, while classical AO systems (Babcock 1953) generally have a small and position-sensitive corrected FOV due to the anisoplanatic angle of the atmospheric turbulence and limited number of bright sources in the sky (Roggemann, Welsh & Hunt 1996).

To extend the AO performance, the use of laser guide stars (LGS) was proposed to generate artificial stars for reference sources (Foy & Labeyrie 1985) and applied to AO-based observations soon after (Fugate et al. 1991). Because LGS can be projected to any position in the sky, the sky coverage is greatly increased. However, the atmospheric turbulence information obtained from LGS is limited by two factors: (1) the tip-tilt mode cannot be detected due to the projection and return paths of LGS; and (2) some atmospheric turbulence cannot be completely detected due to the finite height and number of LGS; this is commonly termed focal anisoplanatism.

The tip-tilt mode is very strong for atmospheric turbulence, and therefore must be otherwise corrected. It can be sensed using a lower-order wavefront sensor (WFS; fewer subapertures if using a Shack–Hartmann wavefront sensor) with a faint natural guide star (NGS) (Rigaut & Gendron 1992). Because the AO-corrected FOV is large in the system under consideration here, the sky coverage problem becomes less serious, i.e. it is highly probable that suitable guide stars can be found within the FOV.

Due to the finite height of the artificial guide star, the volume of atmospheric turbulence sampled will form a cone with an apex at the position of the LGS. Conversely, natural guide stars will probe a cylinder of atmospheric turbulence, the diameter of which will

★ E-mail: robinmartin20@gmail.com (PJ); a.g.basden@durham.ac.uk (AB)

be equal to that of the primary mirror. The difference in sampled volume is therefore responsible for focal anisoplanatism, and leads to reduced LGS performance (Ageorges & Dainty 2000).

The severity of this problem depends on the weight of the undetected error, which is related to the atmospheric turbulence profile. According to *in situ* measurement results from different observatory sites, the majority of atmospheric turbulence is concentrated near ground level (Tokovinin, Baumont & Vasquez 2003; Osborn et al. 2010). If we place several LGS at different locations within the FOV, we can sample and reconstruct most of the atmospheric turbulence at lower heights through the overlapping cones generated by the LGS. Based on this principle, several different wide-field AO methods are proposed according to different observational requirements, such as ground-layer adaptive optics (GLAO), multi-object adaptive optics (MOAO) and multi-conjugate adaptive optics (MCAO).

GLAO concentrates only on compensating atmospheric turbulence near the ground. With suitable overlapping of cones in the ground atmospheric turbulence layer, the angular distance between LGS can become much larger, leading to a uniformly modest correction over a very large field of view (Rigaut 2002; Tokovinin 2004). During the discussion procedure of scientific aims for the *LOT*, Chinese scientists have highlighted a requirement for uniform AO correction over a wide FOV. Due to this requirement, GLAO was considered in the initial science proposal stage for the *LOT* and will become one of the most important components for the Nasmyth system. According to the scientific requirements, after GLAO correction, the images should have a uniform point-spread function (PSF) with a full width at half maximum (FWHM) of 0.20–0.30 arcsec over a 14-arcmin field for wave bands between 0.9–2.4 um.

In this paper, we will first analyse the PSF properties before and after GLAO correction. Then we will propose a FOV-related evaluation factor to analyse some of the key problems of the GLAO systems, including the number of actuators for the deformable mirror, the number, position, power and projection positions of LGS, and mis-conjugation of the DM with respect to the ground-layer atmospheric turbulence and the tilt problem of the DM with respect to the telescope primary axis. Additionally, as there are currently not enough turbulence-profile data from the candidate sites, we will propose a geometric model to show the sensitivity of the GLAO system parameters to different turbulence profiles and give some advice for future site-testing data requirements. Our simulation is based on the Durham Adaptive Optics Simulation Platform (DASP), which has already been used and verified for over 10 years (Basden et al. 2007, 2018).

2 PERFORMANCE EVALUATION FOR THE GLAO SYSTEM

Although the scientific requirements for the GLAO system on the *LOT* have been stated in Su et al. (2017), we still need to propose our performance evaluation factor for the following reasons:

(1) The PSF after GLAO correction is not simply a rescaled seeing-limited one and it is not safe to evaluate the GLAO performance only with the FWHM. We will analyse the PSF properties in Section 2.1 and use several different parameters to evaluate the performance of the GLAO system for different kinds of observations.

(2) As the atmospheric turbulence is stochastic both in the temporal and spatial domains, the final performance of a GLAO system will fluctuate. We will propose a long-time-averaged, FOV-related performance evaluation factor in Section 2.2.

2.1 PSF properties after GLAO correction

Several different observations will give different requirements for this GLAO system. Some of the most common observations are considered here: wide-field imaging, integral field spectrography, astrometry and photometry. The size and shape of PSF are important for imaging. For integral field spectrography, the size of a PSF with a predefined encircled energy is more useful. For multi-object astrometry and photometry, we need to consider the signal-to-noise ratio increase in a fixed exposure time. It is necessary to analyse the PSF properties and select some parameters for performance evaluations. Besides this, we also need to know the potential risks if we evaluate GLAO performance with these parameters.

The FWHM and ellipticity are commonly used to evaluate the PSF size and shape. We use equation 1 to find θ as the FWHM:

$$\text{PSF}(\theta) = 0.5 \times \max(\text{PSF}). \tag{1}$$

We use the Kaiser–Squires–Broadhurst model (Kaiser, Squires & Broadhurst 1995; Heymans et al. 2006) to calculate e_1 and e_2 with equation 2 to describe the ellipticity of the PSF around the centre (x_c, y_c)

$$e_1 = \frac{(Q_{11} - Q_{22})}{(Q_{11} + Q_{22})},$$
$$e_2 = \frac{2Q_{12}}{(Q_{11} + Q_{22})}, \tag{2}$$

where Q_{ij} are the unweighted quadrupole moments

$$Q_{11} = \int \text{PSF}(x, y)(x - x_c)^2 \mathrm{d}x\mathrm{d}y,$$
$$Q_{12} = \int \text{PSF}(x, y)(x - x_c)(y - y_c)\mathrm{d}x\mathrm{d}y,$$
$$Q_{22} = \int \text{PSF}(x, y)(y - y_c)^2 \mathrm{d}x\mathrm{d}y. \tag{3}$$

Meanwhile, we also use D50 (the size of the PSF where 50 per cent of the total energy is encircled) for spectrography and ENA (equivalent noise area) defined in equation 4 for photometry and astrometry evaluation:

$$\int_{\text{centre}}^{\text{D50}} \text{PSF}(\theta_i)\mathrm{d}\theta_i = 0.5 \int_{\text{centre}}^{\infty} \text{PSF}(\theta_i)\mathrm{d}\theta_i,$$
$$\text{ENA} = \frac{1}{\int_{\text{centre}}^{\infty} \text{PSF}^2(\theta_i)\mathrm{d}\theta_i}. \tag{4}$$

To improve the analysis of the PSF properties after GLAO correction, we have carried out three Monte Carlo simulations with different random numbers for a GLAO system in bad seeing conditions with the parameters defined in Table 1, except that the DM has 36×36 actuators. The preliminary results reveal the following properties:

(1) The images of the mean PSF before and after GLAO correction are shown in Fig. 1 along with their 1D profiles.

We can find that the shape of the 1D profile of the PSF after GLAO correction is different from the seeing-limited one. We fit these two curves with the 1D Moffat model defined in equation 5:

$$\text{PSF}(x) = \frac{F(\beta - 1)}{\pi \alpha^2}[1 + (x/\alpha)^2]^{-\beta}; \tag{5}$$

F is the total flux, α is the scale radius and β is a dimensionless parameter. The uncorrected PSF has β of 2.562 and the GLAO-corrected PSF has β of 1.379. According to Vakili & Hogg (2016), the shape of the GLAO-corrected PSF has better properties for astrometry and photometry with the same background noise. However,

Table 1. Initial parameters for the GLAO system.

Parameter	Value	Comment
Telescope diameter	12 m	Central obstruction ratio 0.35, FOV 420 arcsec
Number of actuators in DM	6×6	Conjugate to -88 m, parallel to atmospheric turbulence
Number of subapertures in WFS	5×5	Shack–Hartmann with smaller pixel scale[a]
LGS number	5	Sodium (589 nm), on a circle of 420 arcsec, projected from back of DM
NGS number	3	640 nm, evenly spaced on a circle of 420 arcsec
Atmospheric turbulence	2 layers	Height: 0.15, 10 km; strengths: 70%, 30%
Fried parameter (r_0)	0.2454 m (normal seeing)	0.1431 m (bad seeing), 0.3436 m (good seeing)
Outer scale	10 m	
Reconstruction method	Pseudo inverse	Condition number 0.05
AO control method	Proportional controller	Loop gain 0.5
Simulation result evaluation	FWHM at 840 nm	113 ($15 \times 8 - 7$) science evaluation directions as shown in Fig. 2

[a]Optimized with a smaller pixel scale as discussed in Basden & Morris (2016) with the flux in each WFS subaperture at each time step being about 10^{10} photons (default value in a GLAO system generated by DASP to ensure high-light-level performance).
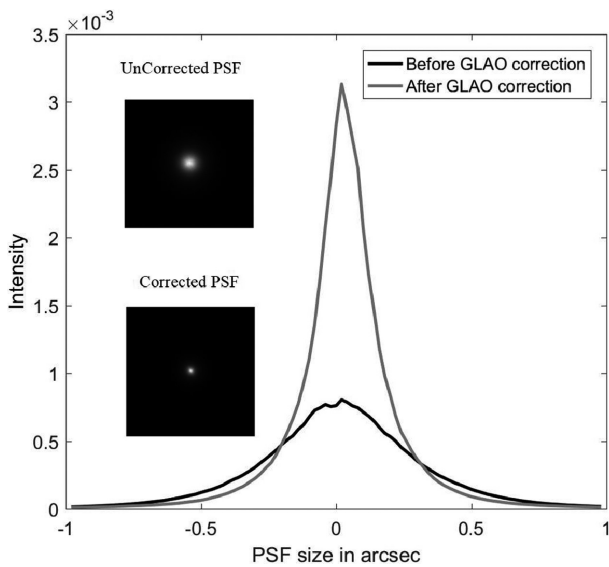
Figure 1. Seeing limited PSF and PSF after GLAO correction for bad seeing conditions. These PSFs are flux normalized and are average of all the PSFs in different positions of the FOV.

the difference of β also indicates that the FWHM may underestimate the full size of the PSF, which will be important for back-end equipment design.

(2) The distribution of the PSF ellipticity is shown in Fig. 3 and we can find that the GLAO system is good at maintaining the shape of the corrected PSF (e_1 and e_2 have been reduced to smaller than 5 per cent). So we will assume that the PSF shape is almost the same for different configurations and only use FWHM to evaluate the PSF shape. In some special cases, such as the GLAO system with a tilted DM, we will use ellipticity and FWHM to evaluate the GLAO performance.

(3) We compare the ratio of FWHM, D50 and ENA between corrected PSF and uncorrected PSF in Figs 4, 5 and 6. We can find that the FWHM increase is larger than that of D50 and ENA. This is because the D50 and the ENA describe the cumulative energy distribution and are more stable to stochastic variation brought about by Monte Carlo simulation and PSF variation. For this reason, we will use FWHM and D50 for performance evlauation of the GLAO system with different configurations. At the end of this paper, we will give the performance of GLAO with all these parameters for

back-end equipment design. Additionally, the distributions of the D50 and FWHM are different, which indicates that a trade-off is required when we use these parameters for GLAO performance evaluation.

(4) We also find that the FWHM is very sensitive to the size of the outer scale, as shown in Fig. 7. We select the outer scale to be 10 m in this paper. If the outer scale is larger, the GLAO performance will drop. For this reason, the outer scale needs to be given special attention and carefully measured during the site-testing stage. We will give the GLAO performance at the end of this paper with outer scales of 10 m and 25 m, respectively.

2.2 GLAO performance evaluation

The scientific requirements require the GLAO system to deliver moderate correction with good uniformity across the full FOV. However, the wide FOV makes the ordinary root mean square or standard variance inadequate here, because these statistical parameters cannot reveal the relative weight for different FOV and will be affected by some unimportant anomalous PSF. We will sample several PSF from different positions within the FOV (as shown in Fig. 2) and propose the following evaluation index:

(1) FWHM reduction ratio FWHM_δ and D50 increase ratio $\mathrm{D50}_\delta$ defined by equation 6:

$$\mathrm{FWHM}_\delta(r) = \frac{\mathrm{FWHM}(r)}{\mathrm{FWHM}'(r)},$$
$$\mathrm{D50}_\delta(r) = \frac{\mathrm{D50}'(r)}{\mathrm{D50}(r)}, \qquad (6)$$

where $\mathrm{FWHM}'(r)$ ($\mathrm{D50}'(r)$) and $\mathrm{FWHM}(r)$ ($\mathrm{D50}(r)$) are the FWHM and the D50 of the PSF before and after GLAO correction in a position with r angular distance to the FOV centre. FWHM_δ can reveal the image-quality improvement in one position of the FOV; as the value becomes lower, the FWHM will be smaller and the performance will be better. $\mathrm{D50}_\delta(r)$ can reveal the encircled energy improvement in one position of the FOV; as the value becomes larger, the D50 will be smaller and the performance will be better.

(2) To show the total performance improvement across the whole FOV of one configuration state (parameter state), we will discretize the FOV into a series of sample points and evaluate the $\mathrm{FWHM}_\delta(r)$ and $\mathrm{D50}_\delta(r)$ at each point r_n. These ratios will be averaged according to the area (ring) defined by two adjacent sample points and used
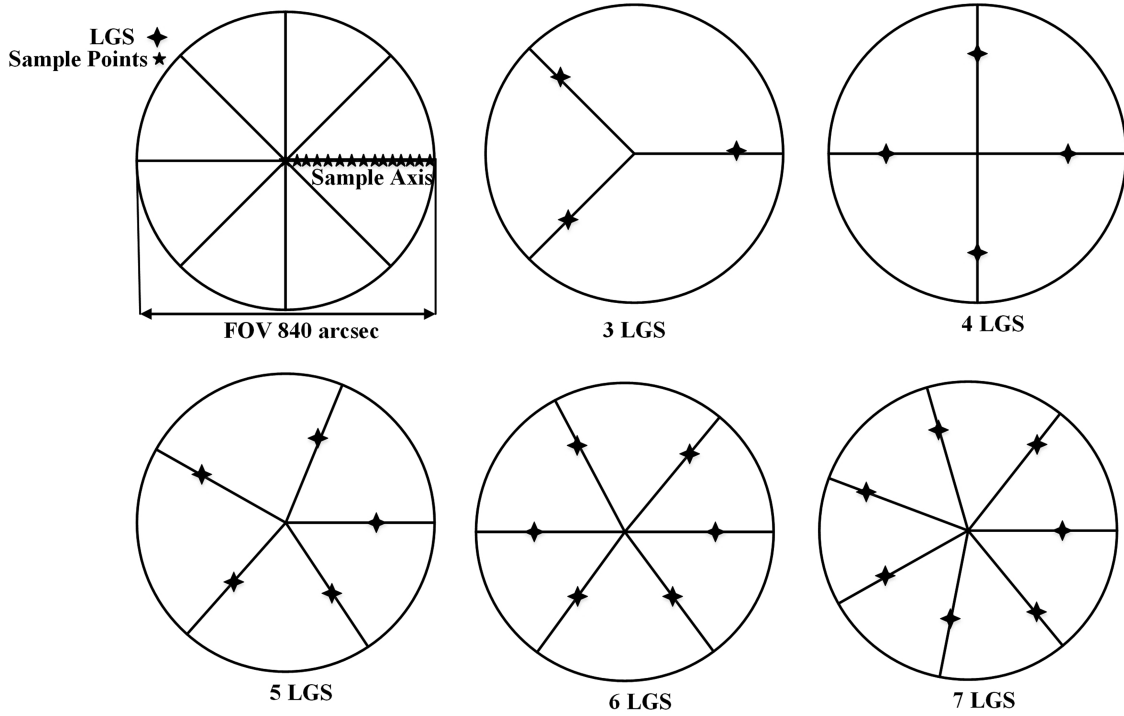
Figure 2. Diagram of the GLAO FOV, sample points and different LGS configurations. 15 sample points are distributed uniformly along the sample axis and there are eight sample axes in the FOV (only some of these science directions in the sample axis are shown here). The total number of science-evaluation directions is 113 (120 - 7) for one simulation. This figure shows different LGS configurations; all the adjacent LGS have equal angular distances between each other for simplicity, i.e. they are placed uniformly on a circle. The LGS are placed 360 arcsec from the centre of the FOV in this figure.
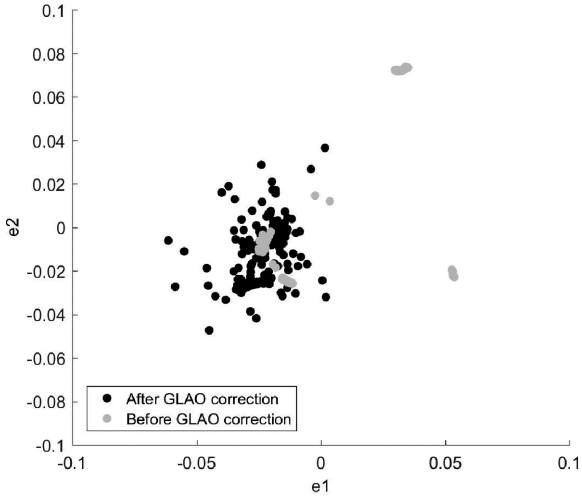
Figure 3. The ellipticity distribution of all the PSF before and after GLAO correction. Results from three simulations with different wind directions and initial random seeds are shown here. We can find that the GLAO system can maintain the PSF with a relatively stable shape regardless of the turbulence condition. The variation of the PSF shape is controlled near 5 per cent while the uncorrected PSF has a shape variation of about 10 per cent.

Figure 4. The distribution of the ratio of the FWHM between the corrected and uncorrected PSF. The star stands for the LGS and the circle stands for the science aim. It is apparent that the best correction can be obtained at the centre of the FOV and there are variations inside the FOV.

(3) To show the correction uniformity, we will therefore show the best and worst performance evaluation factors of all the sample points in one configuration. The GLAO performance is more uniform across the FOV if the difference between the best and worst performances is smaller. In some cases, the fluctuation of GLAO correction in different positions within the FOV will generate extraordinary values. The performance of any GLAO configuration is better if the field-averaged evaluation factor is closer to the best one.

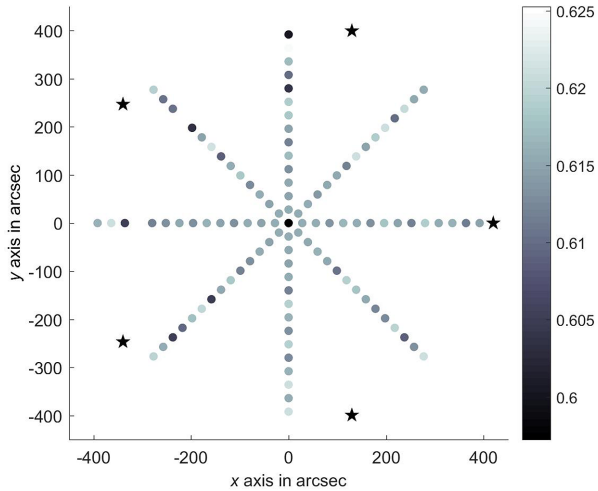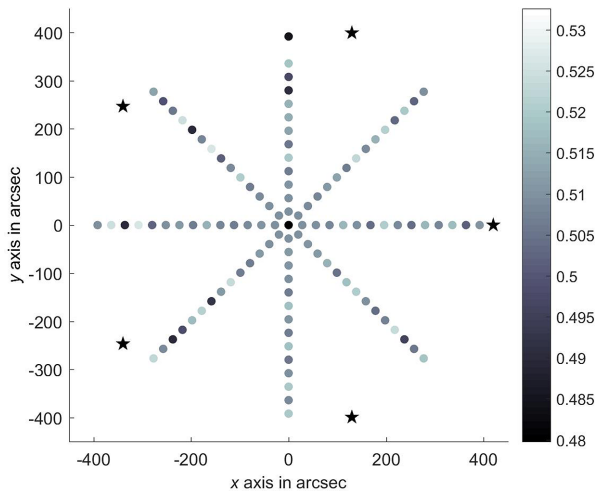in the performance evaluation of one configuration as defined by equation 7:

$$\overline{\text{FWHM}_\delta} = \frac{\sum_{n=2}^{n=N}(r_n^2 - r_{n-1}^2) \cdot \text{FWHM}_\delta(r_n)}{r_N^2},$$

$$\overline{\text{D50}_\delta} = \frac{\sum_{n=2}^{n=N}(r_n^2 - r_{n-1}^2) \cdot \text{D50}_\delta(r_n)}{r_N^2}. \tag{7}$$

Figure 5. The distribution of the ratio of the D50 between the corrected and uncorrected PSF. The star stands for the LGS and the circle stands for the science aim. Compared with the FWHM, the D50 has a smaller increment in performance; however, the variation is smaller and the correction results are more uniform.
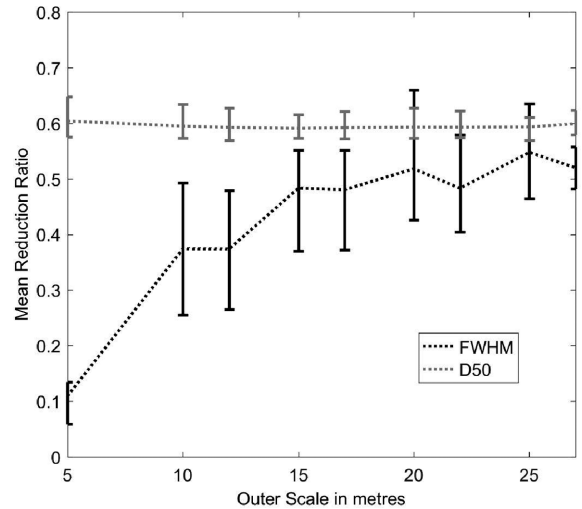

Figure 7. The mean reduction ratio of FWHM and D50 for the same GLAO system with different outer scales. It is apparent that the FWHM is very sensitive to the outer scale when the size of the outer scale is very small and we need to pay special attention to the outer scale for the GLAO system during site testing.

Figure 6. The distribution of the ratio of the ENA between the corrected and uncorrected PSF. The star stands for the LGS and the circle stands for the science aim. The ENA shows a reduction in the required exposure time (required number of photons) for photometry and astrometry after GLAO correction. However, the distribution of ENA is different from that of FWHM and D50.

(4) Because the atmospheric turbulence has stochastic properties in the temporal domain, we run our simulation codes with 12 500 iterations to get the temporal average performance. The time step for each iteration is 0.004 s, and so the total simulation time is 50 s. With these simulations, we can get a well averaged PSF that is not significantly affected by the randomness of simulated atmospheric turbulence phase screens.

According to the above evaluation criteria, we will judge whether a particular AO system design is better than others according to the following rules:

(0) The FWHM is more sensitive to GLAO systems with different parameters and D50 can provide a better reference for back-end

equipment design. We will consider these two factors at the same time and make trade-offs when it is necessary.

(1) The field-averaged performance evaluation factors ($\overline{\mathrm{FWHM}_\delta}$, $\overline{\mathrm{D50}_\delta}$) are the most important evaluation factors: a good AO system design configuration should have a field-averaged performance evaluation factor whose value is less than 0.95 times that in other designs.

(2) When the difference between the field-averaged performance evaluation factors is small, we will select a configuration with a smaller difference between the best and worst performance evaluation factors.

(3) When the difference between the best and worst performance evaluation factors is not significant, we will select a configuration with a field-averaged performance evaluation factor that is closer to the best performance evaluation factor.

(4) For two configurations with similar performance (difference less than 5 per cent), the design configuration with a simpler structure is better; for example, a deformable mirror (DM) with fewer actuators, or a LGS with less flux (reduced laser power).

3 GLAO PARAMETER PROPERTIES AND CONFIGURATION OPTIMIZATION METHOD

A lack of sufficient turbulence-profile data introduces uncertainty into the final GLAO system design, especially for some parameters that are directly related to the turbulence profile. Accumulating enough turbulence-profile data takes a long time. However, in the early design stage, it is necessary to constrain the GLAO parameters for the whole optical design and budget analysis. To fulfil this task, we need to analyse the properties of the GLAO parameters, and constrain some of these parameters if possible. When sufficient turbulence-profile data become available, our analysis can provide a reference for further parameter selection.

We split the GLAO parameter space into two different sets: eigen-parameters and turbulence-profile-related parameters. For a particular GLAO system with different turbulence profiles, when we change the eigen-parameters, the AO performance will show the

same trends. If we investigate the eigen-parameters with a bottom-up search tactic (as we will discuss in Section 3.1), we can constrain a particular scale for the eigen-parameters.

The parameters related to the turbulence profile have complex relationships with different turbulence profiles. However, it is still possible to set these parameters if we know the variation in the trend of the performance of the GLAO system in different turbulence profiles. Obtaining this trend will require a huge amount of simulation with different turbulence profiles. To accelerate the search speed, we propose a geometric model in Section 3.2. Then, we are able to use the Monte Carlo simulation results and the geometric model prediction for parameter selection.

3.1 GLAO parameter search tactic

The selection of a design configuration from a multi-dimensional parameter space of a GLAO system will raise an optimization problem known as the curse of dimensionality (Bellman & Dreyfus 2015). In previous papers about AO configuration design, different parameters are separately considered for performance analysis (Andersen et al. 2006; van Dam et al. 2010; Basden et al. 2012; Wang, Andersen & Ellerbroek 2012; Basden et al. 2013; Jia & Zhang 2013a, b; Oya et al. 2014; Basden & Morris 2016). The parameter-separation method proves effective and we will integrate this method with a bottom-up design concept in our work:

(1) The number of actuators of the DM is an eigen-parameter. We will start with a very simple GLAO system generated by the DASP default GLAO system generator as shown in Table 1 and a simple atmospheric turbulence model with two layers of atmospheric turbulence to simulate the DM correction ability with different numbers of actuators.

(2) The LGS configuration is the most important parameter related to the turbulence profile for the *LOT*. We will first investigate the error induced by the wavefront measurements with a simplified geometric model and many different detailed turbulence profiles. Then we will simulate the GLAO system with five layers of atmospheric turbulence through Monte Carlo simulation. Through this step, we can provide rough estimates of the parameters in the LGS system.

(3) The position of the DM is another turbulence-profile-related parameter. The essence of this problem lies in the relative relation between the conjugation position of the DM and that of the ground-layer turbulence. We will use a detailed atmospheric turbulence model (ESO standard 35-layer model from Sarazin et al. 2013) to evaluate two different GLAO systems: a GLAO system with a DM that is conjugated to different heights and a GLAO system with a tilted DM. All these simulations will be carried out under three different seeing conditions (good seeing, normal seeing and bad seeing with Fried parameters of 0.3436 m, 0.2454 m and 0.1431 m at 840 nm).

Our GLAO system design does not have a prototype or well determined components with detailed parameters, and many parameters are very sensitive and mutually correlated. It is therefore possible to obtain a design configuration with some parameters meeting unnecessarily high specifications. To make sure that every increment in component complexity will give the most benefit to the overall GLAO performance, we will start with the simplest structure or components, and then increase the component complexity to a overall cost or contemporary technology limited value. As the component complexity increases, the GLAO performance will generally improve and we will get an AO performance versus parameter-value
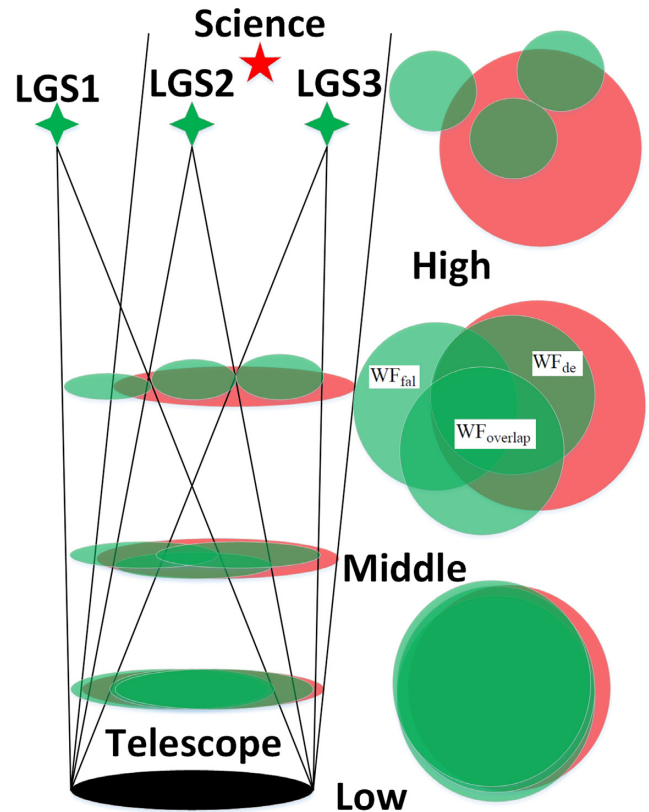
Figure 8. Diagram of a GLAO system. The projection circles of the LGS are plotted in green and those of the science direction are plotted in red. As the height of the turbulence layer increases, WF_{fal} will increase and WF_{de} will decrease.

relationship chart. In this chart, we can find parameters where the inflection point is located. The inflection point indicates a configuration whose performance will not increase significantly as the complexity increases. If, at that inflection point, the GLAO performance still satisfies the scientific requirements, we will select that parameter as the final parameter for the whole system.

3.2 Geometric model for fast GLAO performance evaluation

We propose a geometric atmospheric turbulence model to better estimate the GLAO performance with different turbulence-profile-related parameters. The atmospheric turbulence is simplified to multiple layers in this model. Each layer is placed at height h with normalized $C_n^2(h)$ obtained from the turbulence-profile data. The WFS is able to obtain a turbulence-induced wavefront in each layer and the GLAO system will correct the average of the measurements from different WFS.

A diagram of the GLAO system is shown in Fig. 8. We find that only the region overlapped by the science and the LGS can provide a positive contribution to the GLAO correction. The measurements outside the science (falsely detected) will make a negative contribution to the GLAO correction, because the wavefront from the falsely detected area has almost no relation to that from the science, and correction of that wavefront will reduce the performance. We define WF (the fraction of the wavefront) as the value at the sample point in each turbulence layer and set the WF inside the overlapped region

as 1 and the WF inside the falsely detected region with equation 8:

$$\mathrm{WF}(d) = 1 + b \cdot \left(\frac{d}{r_0}\right)^{\frac{5}{6}}, \tag{8}$$

where d is the distance between the sample point and the nearest point in the science path and r_0 is the atmospheric coherence length. We set WF to be -1 when d is equal to or larger than L_0. Then we will get b for our model. In this paper, L_0 is 10 m and r_0 is 0.1431 m.

The overall fraction of the wavefront that we obtain in a layer at height h can be evaluated by the following equation:

$$\mathrm{WFGain}(h) = \mathrm{WF}_{\mathrm{de}} + \mathrm{WF}_{\mathrm{fal}} - P \cdot \mathrm{WF}_{\mathrm{overlap}}; \tag{9}$$

as shown in Fig. 8, $\mathrm{WF}_{\mathrm{de}}$ and $\mathrm{WF}_{\mathrm{fal}}$ is the sum of WF in the detected and falsely detected areas, respectively, $\mathrm{WF}_{\mathrm{overlap}}$ is the sum of WF in the area that is detected by all LGS, and P is a percentage that reflects the importance of the LGS FOV coverage. Because the GLAO system has a large FOV, we will distribute LGS to ensure that they can cover every part of the field with equal weight as it is not sensible to use all LGS to sample the same area. For this reason, we set P to be 50 per cent in this paper, because we want every pair of the LGS to cover different parts of the FOV.

According to the GLAO wavefront reconstruction method, the measured wavefronts from different LGS will be averaged. After we get WFGain(h), we can normalize this value by the size of the circle projected by the science direction ($A(h)$) in this layer and the number of LGS (N). Then we will have the following relations for all the LGS in a layer with height h:

$$\mathrm{WF}_{\mathrm{de}} = \frac{1}{N \cdot A(h)} \sum_{n=1}^{n=N} \mathrm{WF}_{\mathrm{de}_n}(h),$$

$$\mathrm{WF}_{\mathrm{fal}} = \frac{1}{N \cdot A(h)} \sum_{n=1}^{n=N} \mathrm{WF}_{\mathrm{fal}_n}(h),$$

$$\mathrm{WF}_{\mathrm{overlap}} = \frac{1}{N \cdot A(h)} \prod_{n=1}^{n=N} \mathrm{WF}_{\mathrm{de}_n}(h), \tag{10}$$

where $\mathrm{WF}_{\mathrm{de}_n}(h)$ and $\mathrm{WF}_{\mathrm{fal}_n}(h)$ are the sums of WF in the detected area and in the falsely detected part of the n LGS, respectively. WF-Gain(h) reflects the fraction of reliable wavefront contained in the measurement from the wavefront sensor. WFGain(h) for different science directions with different LGS configurations and different turbulence profiles is shown in Fig. 9. We find that as the height or distance between the science directions and LGS increases, the contribution of $\mathrm{WF}_{\mathrm{fal}_n}(h)$ will increase and that of $\mathrm{WF}_{\mathrm{de}}(h)$ will reduce, which will lead to poorer correction in that layer.

To obtain a uniform correction, we need to balance the contributions of WFGain between different science directions in all the turbulence layers. According to the turbulence profile, we can get the whole atmospheric turbulence contribution to one science direction with the following equation:

$$\mathrm{WFGain} = \sum_{h=h_l}^{h=h_h} \mathrm{WFGain}(h) \cdot C_n^2(h), \tag{11}$$

where $C_n^2(h)$ is the normalized refractive structure index and h_l and h_h are the minimum and maximum height where the turbulence profile is measured. We can represent the GLAO performance with the production of WFGain from several science aims and the FOV-related weights as defined in equation 12:

$$\overline{\mathrm{WFGain}} = \frac{\sum_{n=2}^{n=N} (r_n^2 - r_{n-1}^2) \cdot \mathrm{WFGain}(\theta, r_n)}{r_N^2 \times M}, \tag{12}$$
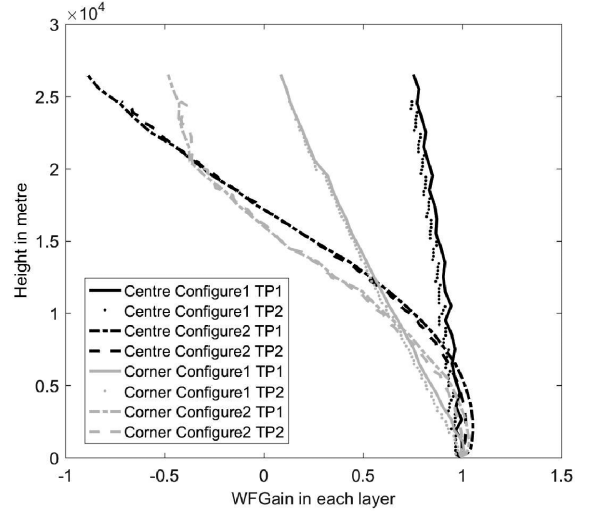
Figure 9. The WFGain(h) for different science directions with different turbulence profiles and different LGS configurations. Centre represents a science target in the centre of the FOV and Corner represents a science target 300 arcsec from the centre of the FOV. Configure 1 and Configure 2 represent five LGS distributed in the way defined in Fig. 2, with an asterism radius of 60 arcsec and 420 arcsec, respectively. TP1 and TP2 represent the first quartile of the ESO 35-layer turbulence-profile model and the turbulence profile from Paranal (Osborn et al. 2016).

where r_n is the distance between the science evaluation directions and the centre of the FOV, M is the total number of science directions and θ is the angle between the science direction and the polar axis. In this part, we will use eight discrete sampling axes and 15 sample points along each axis for different FOV sampling, both with uniform distances, as shown in Fig. 2.

4 NUMBER OF ACTUATORS FOR THE DEFORMABLE MIRROR

In the current *LOT* design, M2 will be a DM with a diameter of 1.81 m and thousands of actuators. The large size and large number of actuators in this DM make it the most expensive and important component in the whole GLAO system. Since this DM is one of the basic components for the *LOT*, manufacturing will begin at an early stage. Once the manufacturing process of that DM begins, the number of actuators will then be fixed. Therefore, in the initial design study, the number of actuators in this DM should be studied according to the scientific requirements, and a clear recommendation provided.

In this section, we will investigate the number of actuators of the DM in a simple model of the GLAO system as given in Table 1 and evaluate its performance. For AO systems, the number of actuators and the number of subapertures in the WFS have a fairly direct relationship. In our simulations, we set the number of subapertures equal to the number of actuators minus one (Fried geometry). With this assumption, the simulation results are shown in Fig. 10. This figure shows the improvement in GLAO system performance as a function of the number of actuators. We draw the following conclusions:

(1) As the number of actuators increases, the GLAO performance will get better.

(2) With better seeing conditions, the performance inflection point is reached earlier.
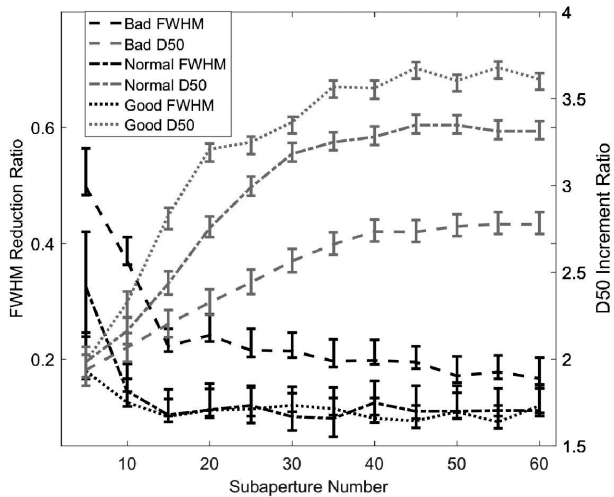
Figure 10. Monte Carlo simulation with a two-layer turbulence model showing the FWHM reduction ratio and the D50 increment ratio versus the number of subapertures (along one direction) for different seeing conditions (given in the legend). The points represent the aperture-averaged parameters $\overline{FWHM_\delta}$ and $\overline{D50_\delta}$ and the error bars are the best and worst results in one configuration.

(3) The benefit of increasing actuator number reduces as the number of actuators increases and when the number of actuators is more than a certain number, there is no increment any more.

(4) There are two choices for the number of actuators. The first one is according to the optimal benefit between the number of actuators and cost: where the slope of the curve between the number of actuators and system performance becomes small (with about 16×16 subapertures for FWHM and 21×21 for D50). The second choice is according to the performance inflection point between the number of actuators and cost: where there are no improvements in the performance, even if we increase the number of actuators (36×36 for FWHM and 41×41 for D50).

According to these simulation results, we suggest that the maximum DM order required should be at most 41×41, because there is then no benefit of increasing the number of actuators further. Also, the DM should have at least 16×16 actuators to give good performance under all seeing conditions, because the slope of the curve around 16×16 is large, which means we will face a risk of low AO performance in the worst seeing conditions or at shorter wavelengths. GLAO with low-order correction is a commonly applied method, but GLAO with high-order correction will benefit further from adaptation of MCAO and other diffraction-limited AO systems and is successfully applied in solar observations (Zhang, Guo & Rao 2017). For these reasons, we will make a trade-off and use a high-order GLAO system with 36×36 actuators for the rest of this study. The FWHM and D50 of PSF after GLAO correction with 36×36 actuators in different seeing conditions is shown in Figs 11 and 12 and it is apparent that the FWHM is not very uniform across the FOV. This is due to the position of the LGS; we will discuss this problem in the next section.

5 LASER GUIDE STAR SYSTEM STUDY

For GLAO systems, LGS are used as references for atmospheric turbulence compensation. A standard model of a sodium laser guide star facility will be considered in this paper with a height of 90 km and a beacon depth of 10 km. As we discussed in Section 1, to get
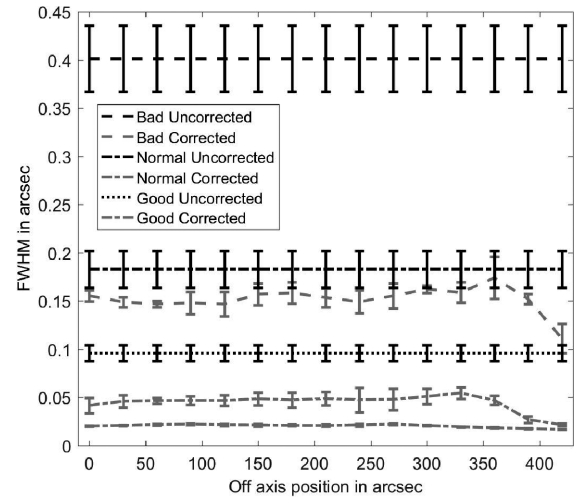
Figure 11. Monte Carlo simulation with a two-layer turbulence model showing the FWHM of PSF across the FOV before and after GLAO correction for different seeing conditions. As shown in this figure, the FWHM after GLAO correction is smaller than 0.2 arcsec. The PSF with the smallest FWHM are around the position of the LGS (420 arcsec).
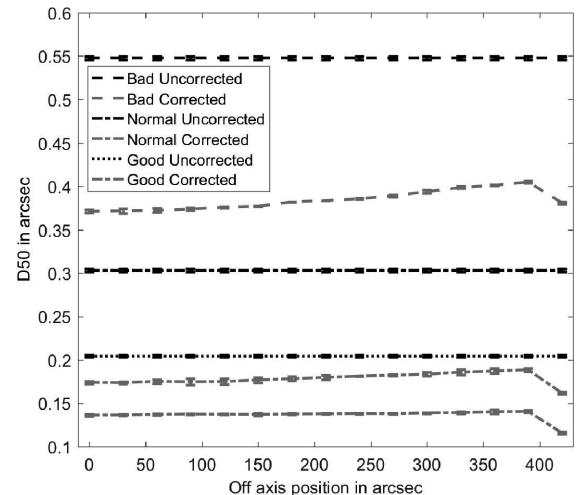
Figure 12. Monte Carlo simulation with a two-layer turbulence model showing the D50 of PSF across the FOV before and after GLAO correction for different seeing conditions. As shown in this figure, the D50 has been reduced by a smaller factor than the FWHM and, in most cases, the D50 is smaller than 0.4 arcsec. The PSF with the smallest D50 are around the position of the LGS (420 arcsec) and the centre of the FOV.

improved AO performance across the whole FOV, multiple LGS will be distributed so as to sample the ground-layer turbulence. The number, position and power of the LGS should be carefully designed to optimize AO performance across the FOV. The LGS launch location (e.g. from behind the central obscuration, or side-launched) also needs to be considered for the whole telescope design.

However, lack of sufficient turbulence data will increase the difficulties of obtaining these parameters. In this section, we will first use several different turbulence-profile data sets and the geometric model to rapidly estimate the sensitivity between the GLAO performance and the turbulence-profile-related parameters. Then we will estimate the GLAO performance of different LGS configura-

Table 2. Five-layer atmospheric turbulence model.

Height in m	Relative weight
150	0.7
2150	0.075
4150	0.075
6150	0.075
8150	0.075

tions through Monte Carlo simulation with a five-layer atmospheric turbulence model, shown in Table 2.

To confirm that this model gives a result in agreement with the true atmospheric turbulence data, we will compare the performance estimate with this model and that with a detailed ESO standard 35-layer atmospheric turbulence profile, and other site-testing data. Two sets of site-testing data are applied for comparison: ESO SCI-DAR data from Paranal from 2016 (Osborn et al. 2016), and Tibet Ali site-testing data from 2011 (Yao et al. 2015). The ESO SCIDAR data were obtained using a Stereo-SCIDAR instrument developed by Durham University (Shepherd et al. 2014). The Tibet Ali site is considered to be one of the best sites in east Asia (Liu et al. 2015a; Ye et al. 2016) and has been selected as one of the potential sites for the *LOT*. The site-testing data are obtained with the method discussed in Liu et al. (2010), Liu et al. (2013) and Liu et al. (2015b). Because this method does not allow ground-layer turbulence measurement, we will set the GLAO system telescope to 100 m lower than the lowest layer of measured turbulence-profile data, and randomly select two nights of site-testing data with different seeing conditions to show the performance variation in these conditions. We also randomly select four seasons of site-testing data from Paranal to check the performance variation. Further detailed statistical analysis will be carried out when there are enough data and we will only describe the preliminary investigation of the LGS system in this paper.

5.1 LGS on-sky position for GLAO

The number and position of LGS have a complex relationship with the final GLAO performance, as shown in Fig. 8:

(1) Increasing the number of LGS will give the GLAO system a more uniform and improved performance, because more wavefront information will be obtained over a large FOV.

(2) By reducing the LGS asterism radius to a certain range, we will reduce the contribution of the falsely detected area and maintain good coverage of the wide FOV of a GLAO system. For a GLAO system working in a typical turbulence profile, there exists an optimal LGS radius.

(3) When multiple LGS are used, we need to distribute the LGS as widely as possible to reduce redundant information.

For these reasons, we will initially use an annular constellation with equal angular distance and measure the relationship between the GLAO system performance and LGS asterism radius. Then we will test GLAO system performance with different numbers of LGS that have the same asterism radius. In this paper, we focus on average improvement in the full FOV and we can reposition the LGS for other scientific requirements, as discussed in Le Louarn & Hubin (2006).

Based on our geometric model, we compute the $\overline{\mathrm{WFGain}}$ for different LGS positions and atmospheric turbulence profiles, as shown in Figs 13, 14 and 15. The results indicate:
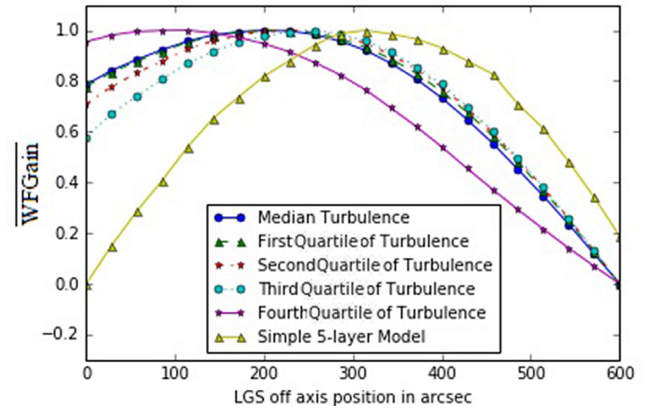

Figure 13. Geometric model showing the $\overline{\mathrm{WFGain}}$ for different LGS positions under the ESO standard 35-layer atmospheric model. As shown in this figure, the $\overline{\mathrm{WFGain}}$ is different for different LGS positions and the optimal position is around 300 arcsec for our simple five-layer model and 200 arcsec for the ESO turbulence profiles. We normalized the $\overline{\mathrm{WFGain}}$ in this figure.
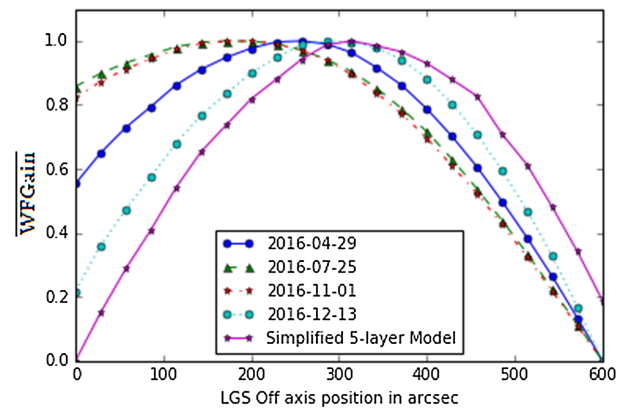
Figure 14. Geometric model showing the $\overline{\mathrm{WFGain}}$ for different LGS positions with Paranal site-testing data. As shown in this figure, for different observation days, the optimal LGS positions change with the turbulence profiles and the performance variation is slow near the optimal LGS position (around 200 to 300 arcsec). We normalized the $\overline{\mathrm{WFGain}}$ in this figure.
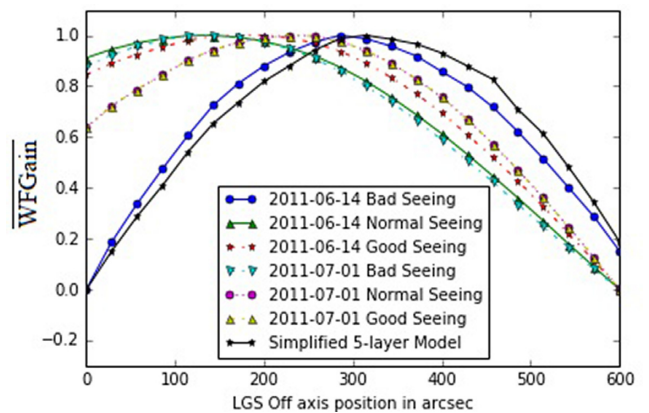
Figure 15. Geometric model showing the $\overline{\mathrm{WFGain}}$ for different LGS positions with Ali site-testing data. As shown in this figure, the optimal LGS position strongly depends on the turbulence profile instead of the seeing conditions, which indicates the importance of detailed turbulence-profile data for the GLAO system. We normalized the $\overline{\mathrm{WFGain}}$ in this figure.
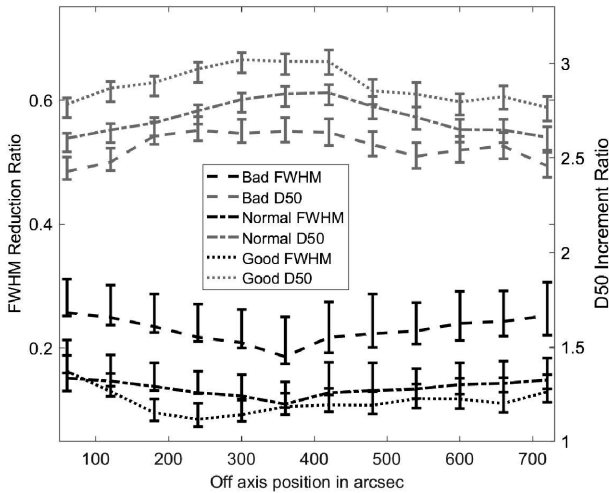
Figure 16. Monte Carlo simulation with a five-layer turbulence model showing the relation between laser guide star position and GLAO performance in different seeing conditions with a five-layer turbulence model. As shown in this figure, when the LGS asterism radius is more than 300 arcsec and less than 400 arcsec, the GLAO system gives the best performance and the slope of the performance curve is small.

(1) The optimal LGS position for GLAO is relatively insensitive when their positions are close to the optimal position. This will reduce the angular accuracy requirement for the LGS projection system in a site with a stable turbulence profile.

(2) Complete turbulence-profile data from the potential site of *LOT* are needed for the optimal position estimation. In this paper, for the five-layer turbulence model, an appropriate LGS asterism radius is around 280 to 360 arcsec and we propose 360 arcsec as an optimal position since we need the asterism radius to encompass as much of the FOV as possible.

The Monte Carlo simulation results support the geometrical model prediction as shown in Fig. 16. Due to the stochastic property of atmospheric turbulence, there are fluctuations in the final performance estimates obtained by Monte Carlo simulation. As the LGS asterism radius increases, the performance increases up to 360 arcsec and the appropriate position for LGS is therefore 360 arcsec for FWHM. For D50, the performance difference is small when the position for the LGS is between 300 and 420 arcsec. We set the position of the LGS to be 360 arcsec, because the variation in GLAO performance is small near this position. The GLAO performance for different seeing conditions is shown in Figs 17 and 18. We can find that the correction result is better in the region near the LGS and by moving the LGS closer to the centre we can get better performance in the overall FOV.

5.2 LGS number for GLAO

With the selected LGS position of 360 arcsec, we compute the $\overline{\text{WFGain}}$ with different numbers of LGS to explore GLAO system performance. As shown in Figs 19, 20 and 21, the $\overline{\text{WFGain}}$ will increase when the number of LGS increases (for a better comparison of different configurations, we set all the curves of $\overline{\text{WFGain}}$ to start from zero), but the benefit is small (the slope of the $\overline{\text{WFGain}}$ curve is between 0.03 LGS^{-1} and 0.0083 LGS^{-1}). In our geometric model we assume that the falsely detected area will still contribute to $\overline{\text{WFGain}}$, which will give a slightly better result for GLAO with more LGS. Considering the increasing cost of LGS as the number
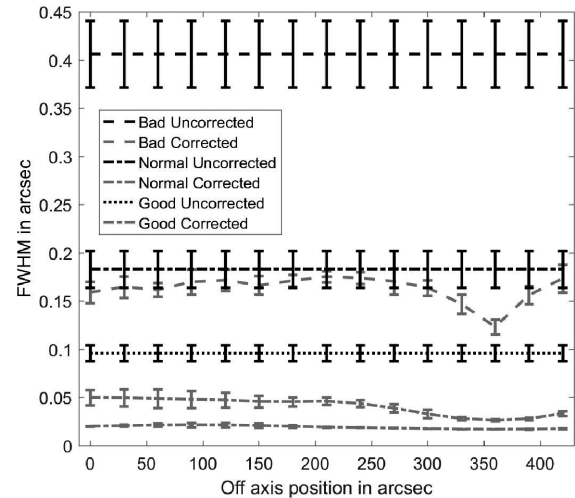

Figure 17. Monte Carlo simulation with a five-layer turbulence model showing the FHWM as a function of position within the FOV, when the LGS are 360 arcsec from the FOV centre. Science targets with the best performance are around the position of the LGS (360 arcsec).
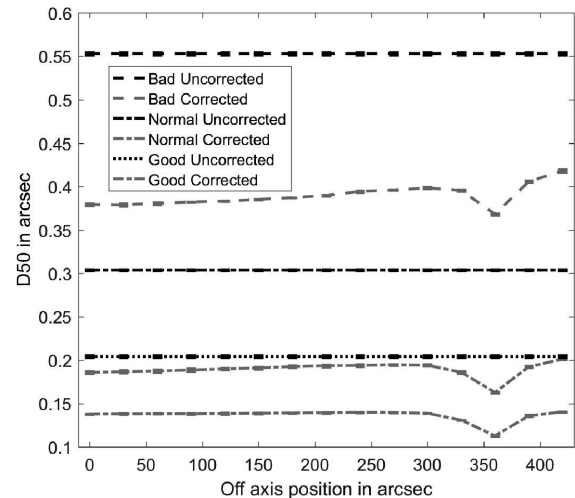

Figure 18. Monte Carlo simulation with a five-layer turbulence model showing the D50 as a function of position within the FOV, when the LGS are 360 arcsec from the FOV centre. Science targets with the best performance are around the position of the LGS (360 arcsec).

of LGS increases and the possible lack of benefit to the overall performance of the GLAO system, we suggest four LGS for our GLAO system.

To check the appropriate number of LGS for our GLAO system, we simulate a GLAO system under different seeing conditions with different LGS numbers. As shown in Fig. 22, the GLAO system will have better performance when the number of LGS is more than four. However, as the performance improvement is not large and a GLAO system with four LGS can still satisfy the scientific requirements, we suggest using four LGS, due to the high cost and complexity of laser guide stars. As shown in Figs 23 and 24, compared with our simulation results of five LGS in Figs 17 and 18, the difference is not significant.
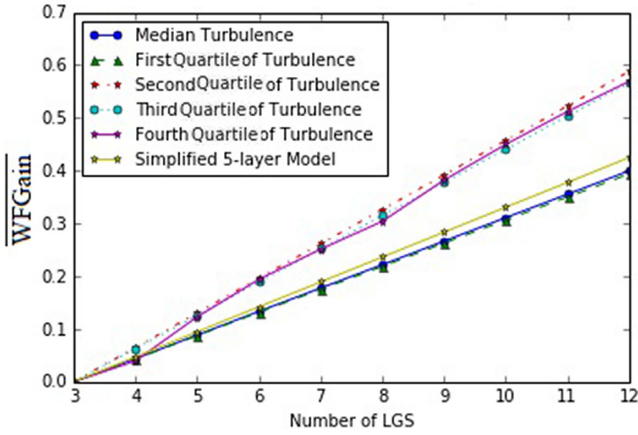
Figure 19. Geometric model showing the $\overline{\text{WFGain}}$ for different LGS numbers using the ESO standard 35-layer atmospheric model. As shown in this figure, the $\overline{\text{WFGain}}$ will increase when the LGS number increases, although the slope of the increment depends on the turbulence profile.
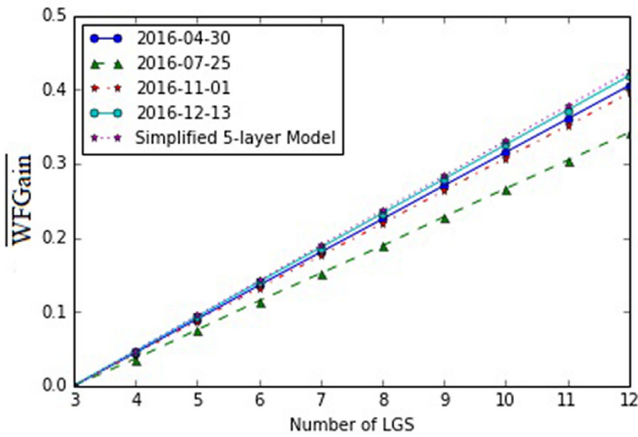

Figure 20. Geometric model showing the $\overline{\text{WFGain}}$ for different LGS numbers under Paranal site-testing data. As shown in this figure, the $\overline{\text{WFGain}}$ will increase when the LGS number increases, although the slope of the increment depends on the turbulence profile.
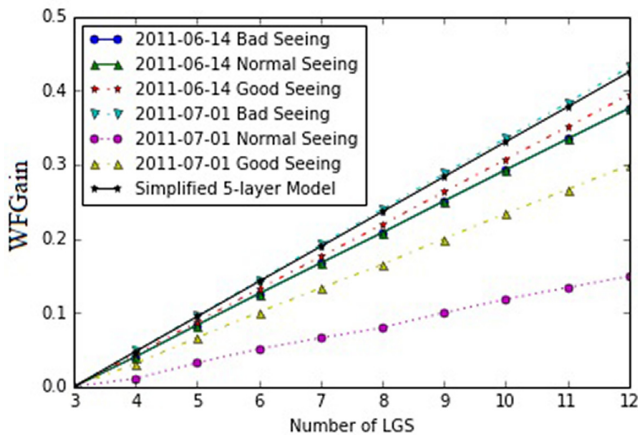
Figure 21. Geometric model showing the $\overline{\text{WFGain}}$ for different LGS numbers under Ali site-testing data. As shown in this figure, the $\overline{\text{WFGain}}$ will increase when the LGS number increases, although the slope of the increment depends on the turbulence profile.
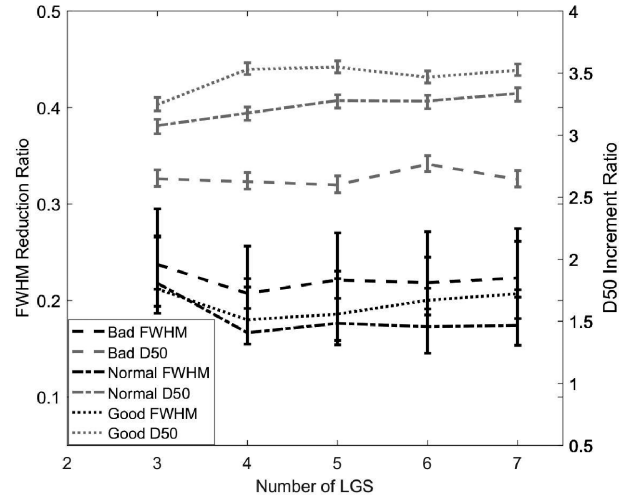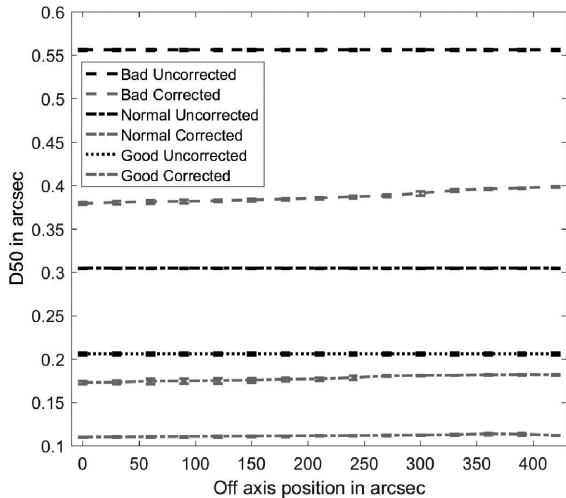

Figure 22. Monte Carlo simulation with a five-layer turbulence model showing the relation between laser guide star number and GLAO performance in different seeing conditions. As shown in this figure, when the number of LGS is more than three, there is no significant performance difference for different LGS numbers.
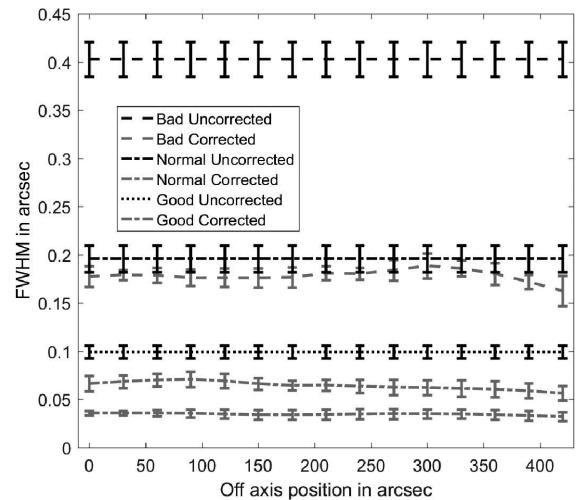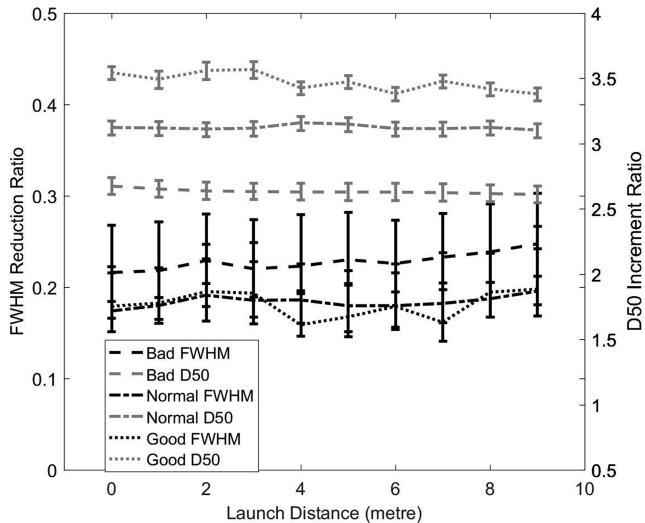

Figure 23. Monte Carlo simulation with a five-layer turbulence model showing the FWHM across the FOV when the LGS is placed 360 arcsec from the centre of the FOV with four LGS. Reduction of LGS number does not significantly reduce the GLAO performance.

5.3 LGS projection method

During observations, LGS will be propagated from the ground-based launch telescope and will generate elongated images within the wavefront sensors (assumed to be Shack–Hartmann based), which are then used for wavefront sensing. The elongation of the LGS image is directly related to the distance between the telescope primary pupil and the laser guide star projection facility (launch telescope). Two projection methods are possible for a GLAO system: projection from behind the telescope secondary mirror or projection from the edge of the telescope. For the first method the maximum distance is 6 m from the centre of the telescope to the furthest subaperture, while for the second method the maximum distance can be more than 12 m. Although these distances are small and will not introduce serious elongation problems, we will also check our GLAO system performance with different distances from the

Figure 24. Monte Carlo simulation with a five-layer turbulence model showing the D50 across the FOV when the LGS is placed 360 arcsec from the centre of the FOV with four LGS. Reduction of LGS number does not significantly reduce the GLAO performance.
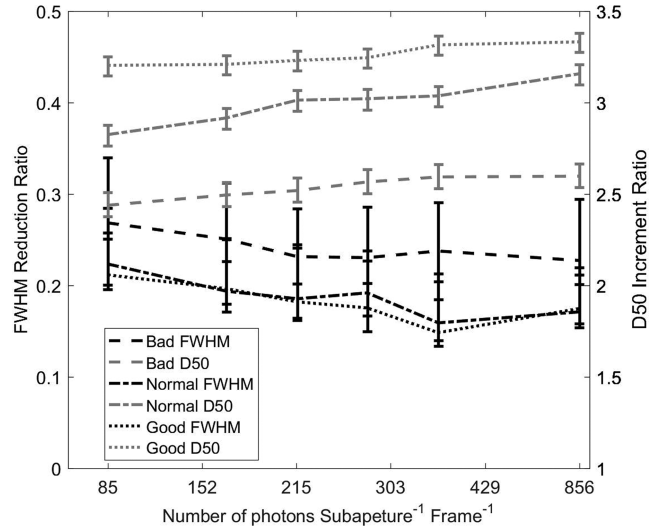

Figure 25. Monte Carlo simulation with a five-layer turbulence model showing the relation between laser guide star launch distance and GLAO performance in different seeing conditions.

LGS projection facility to the centre of the telescope to provide a reference for further telescope design studies. We simulate the GLAO system with different launch distances from the centre of the telescope. As shown in Fig. 25, the relationship between the GLAO system performance and the launch distance is weak if the projection facility is not very far from the telescope mirror.

5.4 LGS power requirements

For the whole telescope budget consideration, the LGS power will be considered here. LGS with different laser powers will generate different numbers of photons in the wavefront sensor. Because the number of photons in the wavefront sensor is related to different LGS and telescope models (throughput etc.) and the sodium layer density, for simplicity, we will use photons subaperture^{-1} frame^{-1} as the measurement of LGS power. For further study of the LGS
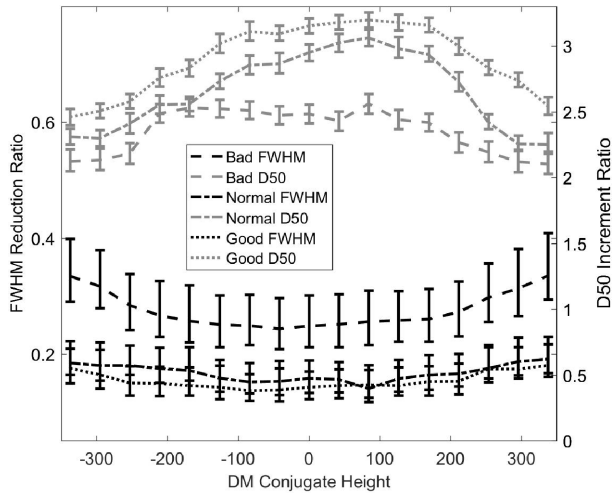

Figure 26. Monte Carlo simulation with a five-layer turbulence model showing the relation between return number of photons per subaperture per frame and GLAO performance in different seeing conditions.

system, the laser power requirement for different types of laser guide stars can be calculated with their individual models, different *in situ* sodium densities (Wei et al. 2016; Feng et al. 2016) and the simulation results discussed in this paper.

As discussed in Clare & Le Louarn (2010), a GLAO system requires fewer photons than other AO systems and a significant improvement can be obtained when the number of photons subaperture^{-1} frame^{-1} is of the order of 100–200. For a 12-m telescope, we refer to their research results and investigate our GLAO system performance with numbers of photons subaperture^{-1} frame^{-1} from 85 to 856. We simulate the GLAO system with Shack–Hartmann wavefront sensors using 35×35 subapertures and a centre-of-gravity (COG) algorithm for the wavefront centroid and we can anticipate better performance with other methods such as a matched-filter method (Gilles & Ellerbroek 2006; Conan et al. 2009; Basden et al. 2017). The LGS are centre-launched from behind the secondary mirror. As shown in Fig. 26, for different seeing conditions, the GLAO performance improves as flux increases, up to about 300–400 photons, after which wavefront sensor noise is no longer the dominant error. We also find that in different seeing conditions, the variance of improvement will increase when the number of photons is reduced, and this is a specific problem for GLAO, which requires a specific wavefront reconstruction method. According to these simulation results, the LGS should provide at least 3.675×10^5 photons frame^{-1} for wavefront sensing ($35 \times 35 \times 300$).

6 DEFORMABLE MIRROR MIS-CONJUGATION AND TILT CONSIDERATION

The deformable secondary mirror in the original *LOT* design is optically conjugated to 88 m below the ground. We now consider this effect in the simulations with different conjugation heights to provide a reference both to the science plan and optical design. We further consider the case where the DM is tilted with respect to the optical axis of the telescope, which is the case when M4 is used as a DM (e.g. in the *European Extremely Large Telescope* (*E-ELT*)), and therefore there can be a few tens of metres difference in the

Figure 27. Monte Carlo simulation with the ESO standard 35-layer turbulence model showing the relation between DM conjugation height and GLAO performance in different seeing conditions. The D50 is more sensitive to the conjugation height. For the optimal conjugate height (around 88 m), D50 has its maximal value. Meanwhile, the sensitivity of the FWHM is reduced by the relatively large variation.
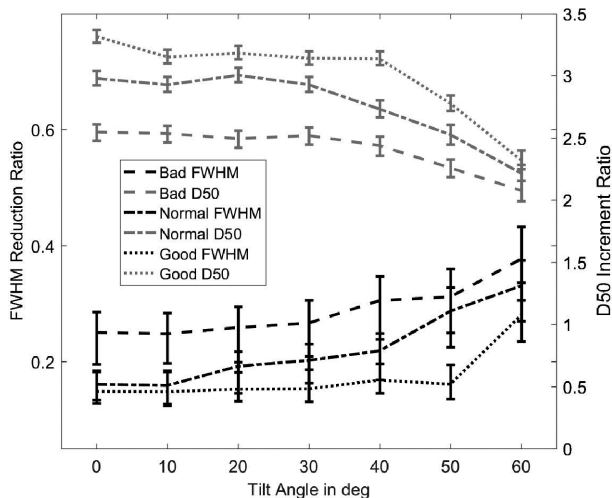

Figure 28. Monte Carlo simulation with the ESO standard 35-layer turbulence model showing the relation between DM tilt angle and GLAO performance in different seeing conditions.

conjugate heights of different actuators. These DM misalignment and tilt problems exist for almost all GLAO systems with a DM of negative conjugate height. We use the ESO standard 35-layer atmospheric turbulence profile in Monte Carlo simulations with different tilt angles of the DM to investigate system performance.

6.1 DM mis-conjugation problem

For the mis-conjugation problem, we simulate the GLAO system with the parameters that we defined in the previous part of this paper, and set the conjugation height of the DM from between -328 m to 328 m. As shown in Fig. 27, when the conjugation height changes, the GLAO performance will be affected. Although the optimal conjugation height is around 88 m in simulation, this does not imply that conjugating to 88 m is a proper choice. The height
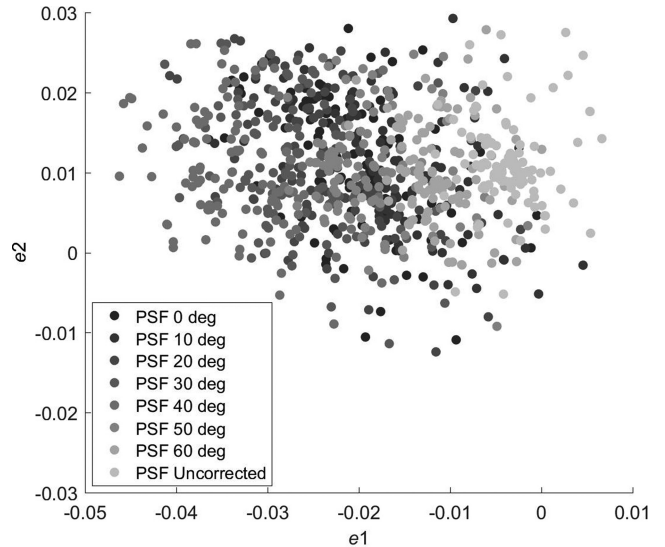
Figure 29. PSF ellipticity variation with different DM tilt angles for a well calibrated GLAO system. Very little difference in ellipticity can be observed.
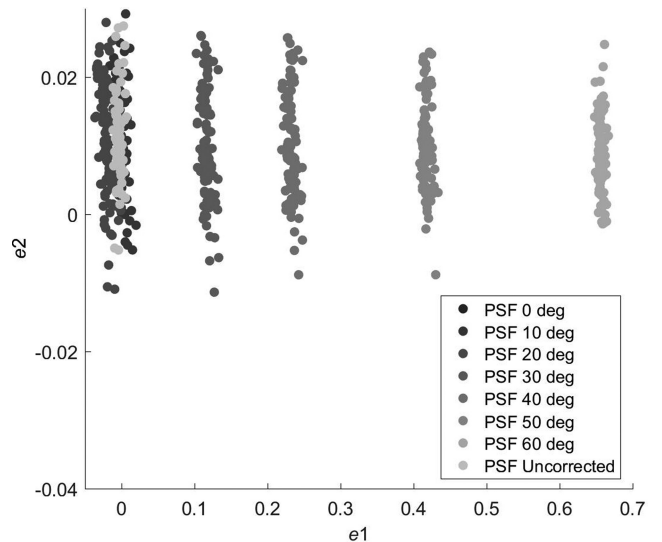
Figure 30. PSF ellipticity variation with different DM tilt angles for an uncalibrated GLAO system. A significant difference in ellipticity can be observed. Because we consider tilt angles with discrete values, the clusters of PSF distribute discretely. For real observations, the ellipticity of PSF will distribute between these discrete values and in different directions, depending on the relative position of the primary mirror and DM. In these circumstances, the DM tilt angle should be smaller than 30 degrees to keep the ellipticity of the corrected PSF smaller than the eigen-ellipticity of all the PSF.

and thickness of ground-layer turbulence will change with time, and the DM conjugation height will change when the telescope points to different zenith angles. For these reasons, these simulation results indicate an error term within the error budget for our GLAO system. Ideally, the conjugation height of the DM should be less than or equal to the height of ground-layer turbulence. We suggest that the DM conjugation height should be between negative 128 m and positive 128 m. The *LOT* GLAO system is required to provide a PSF with a FWHM around 0.2 arcsec, which is a challenging task with bad seeing. For bad seeing conditions, the slope of the curve

Table 3. The performance of the GLAO system with the ESO 35-layer atmospheric turbulence profile at a wavelength of 840 nm. This table shows the mean value and the standard variation of these parameters. The numbers in the brackets are the parameters of seeing-limited PSF and the numbers outside the brackets are the parameters of GLAO-corrected PSF.

Seeing conditions	FWHM in arcsec	D50 in arcsec	ENA in arcsec^2
Good ($L_0 = 10$ m)	0.0454 ± 0.0021 (0.1221 ± 0.0014)	0.1312 ± 0.0027 (0.2148 ± 0.0051)	0.0485 ± 0.0011 (0.1716 ± 0.0007)
Normal ($L_0 = 10$ m)	0.0966 ± 0.0034 (0.1762 ± 0.0043)	0.2108 ± 0.0040 (0.2993 ± 0.0004)	0.1779 ± 0.0007 (0.3838 ± 0.0072)
Bad ($L_0 = 10$ m)	0.2186 ± 0.0077 (0.4006 ± 0.0116)	0.4193 ± 0.0047 (0.5537 ± 0.0014)	0.6961 ± 0.0130 (1.3656 ± 0.0047)
Good ($L_0 = 25$ m)	0.0879 ± 0.0081 (0.1697 ± 0.0186)	0.1438 ± 0.0066 (0.2472 ± 0.0028)	0.0845 ± 0.0074 (0.2607 ± 0.0074)
Normal ($L_0 = 25$ m)	0.1313 ± 0.0088 (0.2539 ± 0.0240)	0.2166 ± 0.0084 (0.3528 ± 0.0024)	0.1966 ± 0.0155 (0.5442 ± 0.0073)
Bad ($L_0 = 25$ m)	0.2624 ± 0.0254 (0.4899 ± 0.0333)	0.4350 ± 0.0110 (0.6216 ± 0.0030)	0.8204 ± 0.0496 (1.8500 ± 0.0246)

between the FWHM and conjugation height of the DM is small between -128 m and 128 m and changes abruptly beyond that.

6.2 DM tilt problem

When the DM is tilted relative to the major axis of the telescope, as is the case for the *ELT* (Delabre 2008), the DM conjugate height will vary across the DM. This tilted DM will reduce the AO correction ability and intensify the mis-conjugation problem. A tilted DM was considered during the design process of the *LOT*. To test our GLAO system performance as well as provide a reference for the optical design, we simulated a DM with a tilt angle from 0 degrees to 60 degrees (relative to the primary mirror) with the DM conjugated to -88 m, projected the DM to an elliptical in the conjugate height and calculated the correction wavefronts according to the tilt angle. The performance of the GLAO system is seen to decrease when the DM is tilted as shown in Fig. 28. The relation between the variation of GLAO performance and that of the tilt angle is not linear. When the angle is smaller than 30 degrees, performance difference is small and when the angle is larger than 45 degrees, the performance drops rapidly.

The shape variation of PSF is another problem that would be introduced by a tilted DM, because, for a secondary DM, the stroke of the actuators is large enough to keep an acceptable correction ability when the tilt angle is small, as we discussed above. Therefore, we will only discuss the PSF shape-variation problem here and assume that the correction ability is not affected. When the DM is tilted, the image quality in the science camera depends on whether the science path and the WFS path can be well calibrated before observations. Inadequate calibration error can be seen as a type of non-common path aberration between the science path and the WFS path. The shape variation of PSF will be between two extremes: well calibrated and uncalibrated. We use the KSB model defined in Section 2.1 to calculate the variation of PSF ellipticity. For a well calibrated GLAO system, the variation of the PSF shape is very small, as shown in Fig. 29. For an uncalibrated GLAO system, the PSF will be stretched in the image plane, as shown in Fig. 30. Considering the two extreme situations above, we recommend that the GLAO system has a DM with a tilt of less than 30 degrees.

7 CONCLUSIONS AND FUTURE WORK

In this paper, using Monte Carlo simulation and geometric model testing with real observatory-site atmospheric profiles, we investigate the GLAO performance for the *LOT*. We have explored a parameter space including the number of DM actuators and wavefront sensor order, the position, number and power of the laser guide stars, their launch location, and misconjugation and tilt effects for the DM. With these results, we provide recommendations

for the GLAO system designs. With the parameters that we selected in this paper, we can anticipate the GLAO performance with the ESO 35-layer turbulence profile, as shown in Table 3. From the simulation results, we find that the GLAO system can satisfy the scientific requirements proposed by Su et al. (2017). We also give the performance evaluation factors with other scientific observation requirements. These simulation results can also be used for further budget and design considerations for the whole telescope, as well as for further discussion of scientific observation plans (Ma & Cai 2017).

Due to the large 14-arcmin FOV of the proposed GLAO system and the large telescope aperture, there is still much work that needs to be further studied. First, although we have defined different metrics for the GLAO performance evaluation of different scientific observations, it still needs improvement: we plan to consider different scientific observations (Basden, Evans & Morris 2014; Salinas et al. 2016; Chun et al. 2016; Mendes de Oliveira et al. 2017; Gavel 2017) and carry out end-to-end observation simulations to generate real observation data for further performance analysis. We will also use some clustering-based PSF evaluation methods (Jia et al. 2017) to better evaluate the GLAO performance. Secondly, we use a standard multi-layer thin atmosphere model for the atmospheric turbulence. However, as the FOV of the GLAO system is large, many issues remain that require study using real site-testing data (Chun et al. 2009; Osborn et al. 2016; Mazzoni et al. 2016; Goodwin, Jenkins & Lambert 2016; Carbillet et al. 2017) and a turbulence phase model with high fidelity and high speed that can reflect the impact of the outer scale (Jia et al. 2015a, b) and non-Kolmogorv turbulence models (Rao, Jiang & Ling 2000).

In particular, there are not enough turbulence data from the candidate sites for the *LOT*, and this should be rectified over the next few years. For a GLAO system, the turbulence profiles are needed to give a full description of the GLAO system performance, especially those with high resolution near the ground layer (Schöck et al. 2009; Tokovinin, Bustos & Berdja 2010). Because GLAO systems are commonly used as seeing stabilizers, which will work with different seeing conditions and with different turbulence profiles, we need to provide the best and worst expected performance estimates of GLAO during observations. These performance descriptions can be used to better improve the plan of scientific observations and the design of other post-GLAO scientific instruments.

REFERENCES

Ageorges N., Dainty C., eds, 2000, Laser Guide Star Adaptive Optics for Astronomy NATO Advanced Science Institutes (ASI) Series C, Vol. 551, Springer Science & Business Media, Dordrecht
Andersen D. R. et al., 2006, PASP, 118, 1574
Babcock H. W., 1953, PASP, 65, 229
Basden A. G. et al., 2017, MNRAS, 466, 5003
Basden A. G., Morris T. J., 2016, MNRAS, 463, 4184
Basden A., Butterley T., Myers R., Wilson R., 2007, Applied Opt., 46, 1089
Basden A., Bharmal N. A., Butterley T., Dipper N., Morris T., Myers R., Reeves A., 2012, in Adaptive Optics Systems III, International Society for Optics and Photonics, Amsterdam, Netherland. p. 84475E
Basden A. G., Bharmal N. A., Myers R. M., Morris S. L., Morris T. J., 2013, MNRAS, 435, 992
Basden A. G., Evans C. J., Morris T. J., 2014, MNRAS, 445, 4008
Basden A., Bharmal N., Jenkins D., Morris T., Osborn J., Jia P., Staykov L., 2018, Software X, 7, 63
Bellman R. E., Dreyfus S. E., 2015, Applied Dynamic Programming. Princeton Univ. Press, Princeton, NJ
Carbillet M., Aristidi ., Giordano C., Vernin J., 2017, MNRAS, 471, 3043
Chun M. R. et al., 2016, in Adaptive Optics Systems V., International Society for Optics and Photonics, . p. 9909
Chun M., Wilson R., Avila R., Butterley T., Aviles J.-L., Wier D., Benigni S., 2009, MNRAS, 394, 1121
Clare R. M., Le Louarn M., 2010, in Adaptative Optics for Extremely Large Telescopes , EDP sciences. p. 03005,
Conan R., Lardière O., Herriot G., Bradley C., Jackson K., 2009, Applied Opt., 48, 1198
Cui X.-q., Zhu Y.-t., 2016, in Society of Photo-Optical Instrumentation Engineers (SPIE) Conference Series, International Society for Optics and Photonics, Edinburgh, United Kingdo m, p. 990607
Delabre B., 2008, A&A, 487, 389
Feng L. et al., 2016, Res. Astron. Astrophys., 16, 144
Foy R., Labeyrie A., 1985, A&A, 152, L29
Fugate R. Q. et al., 1991, Nature, 353, 144
Gavel D., 2017, preprint (arXiv:1706.00041)
Gilles L., Ellerbroek B., 2006, Applied Opt., 45, 6568
Goodwin M., Jenkins C., Lambert A., 2016, MNRAS, 461, 1701
Heymans C. et al., 2006, MNRAS, 368, 1323
Jia P., Zhang S., 2013a, Res. Astron. Astrophys., 13, 875
Jia P., Zhang S., 2013b, Sci. China Phys. Mech. Astron., 56, 658
Jia P., Cai D., Wang D., Basden A., 2015a, MNRAS, 447, 3467

Jia P., Cai D., Wang D., Basden A., 2015b, MNRAS, 450, 38
Jia P., Sun R., Wang W., Cai D., Liu H., 2017, MNRAS, 470, 1950
Kaiser N., Squires G., Broadhurst T., 1995, ApJ, 449, 460
Le Louarn M., Hubin N., 2006, MNRAS, 365, 1324
Liu L. et al., 2013, Chinese Sci. Bull., 58, 4566
Liu L., Yao Y., Vernin J., Wang H., Yin J., Qian X., 2015b, J. Phys. Conf. Series, 595, 012019
Liu L.-Y., Yao Y.-Q., Wang Y.-P., Ma J.-L., He B.-L., Wang H.-S., 2010, Res. Astron. Astrophys., 10, 1061
Liu L.-Y., Giordano C., Yao Y.-Q., Vernin J., Chadid M., Wang H.-S., Yin J., Wang Y.-P., 2015a, MNRAS, 451, 3299
Ma D., Cai Z., 2017, MNRAS, preprint (arXiv:1708.01257)
Mazzoni T., Busoni L., Bonaglia M., Esposito S., 2016, in Adaptive Optics Systems V, International Society for Optics and Photonics, p. 99093R
Mendes de Oliveira C., Amram P., Quint B. C., Torres-Flores S., Barbá R., Andrade D., 2017, MNRAS, 469, 3424
Osborn J., Wilson R., Butterley T., Shepherd H., Sarazin M., 2010, MNRAS, 406, 1405
Osborn J., Wilson R., Butterley T., Morris T., Dubbeldam M., Dérie F., Sarazin M., 2016, in Adaptive Optics Systems V, International Society for Optics and Photonics. p. 99091N
Oya S. et al., 2014, in Adaptive Optics Systems IV, International Society for Optics and Photonics. p. 91486G
Rao C., Jiang W., Ling N., 2000, J. Modern Opt., 47, 1111
Rigaut F., 2002, in Vernet E., Ragazzoni R., Esposito S., Hubin N., eds, European Southern Observatory Conference and Workshop Proceedings Vol. 58, European Southern Observatory Conference and Workshop Proceedings. p. 11
Rigaut F., Gendron E., 1992, A&A, 261, 677
Roggemann M. C., Welsh B. M., Hunt B. R., 1996, Imaging through Turbulence. CRC Press, Boca Raton, FL
Salinas R., Contreras Ramos R., Strader J., Hakala P., Catelan M., Peacock M. B., Simunovic M., 2016, AJ, 152, 55
Sarazin M., Le Louarn M., Ascenso J., Lombardi G., Navarrete J., 2013, in Esposito S., Fini L., eds, Proceedings of the Third AO4ELT Conference. p. 89
Schöck M. et al., 2009, PASP, 121, 384
Shepherd H. W., Osborn J., Wilson R. W., Butterley T., Avila R., Dhillon V. S., Morris T. J., 2014, MNRAS, 437, 3568
Su D.-q., Yu X.-m., Zhou B.-f., 1990, Sci. China A , 4, 007
Su D.-q., Liang M., Yuan X., Bai H., Cui X., 2016, MNRAS, 460, 2286
Su D.-q., Liang M., Yuan X., Bai H., Cui X., 2017, MNRAS, 469, 3792
Tokovinin A., 2004, PASP, 116, 941
Tokovinin A., Baumont S., Vasquez J., 2003, MNRAS, 340, 52
Tokovinin A., Bustos E., Berdja A., 2010, MNRAS, 404, 1186
Vakili M., Hogg D. W., 2016, preprint (arXiv:1610.05873)
van Dam M. A. et al., 2010, Modeling the adaptive optics systems on the Giant Magellan Telescope
Wang L., Andersen D., Ellerbroek B., 2012, Applied Opt., 51, 3692
Wei K. et al., 2016, Res. Astron. Astrophys., 16, 183
Yao Y., Zhou Y., Liu L., Wang H., Yin J., You X., Fu X., 2015, J. Phys. Conf. Series, 595, p. 012038
Ye Q.-Z., Su M., Li H., Zhang X., 2016, MNRAS, 457, L1
Zhang L., Guo Y., Rao C., 2017, Opt. Express, 25, 4356

This paper has been typeset from a T[E]X/L[A]T[E]X file prepared by the author.